Self-gravitating disks around rapidly spinning, tilted black holes: General-relativistic simulations

Antonios Tsokaros[,1,*] Milton Ruiz,[1,2] Stuart L. Shapiro[,1,3] and Vasileios Paschalidis[4]

[1]*Department of Physics, University of Illinois at Urbana-Champaign, Urbana, Illinois 61801, USA*
[2]*Departamento de Astronomía y Astrofísica, Universitat de València,
Dr. Moliner 50, 46100, Burjassot (València), Spain*
[3]*Department of Astronomy and NCSA, University of Illinois at Urbana-Champaign,
Urbana, Illinois 61801, USA*
[4]*Departments of Astronomy and Physics, University of Arizona, Tucson, Arizona 85719, USA*

We perform general-relativistic simulations of self-gravitating black hole disks in which the spin of the black hole is significantly tilted (45° and 90°) with respect to the angular momentum of the disk and the disk–to–black hole mass ratio is 16–28%. The black holes are rapidly spinning with dimensionless spins up to $\sim$0.97. These are the first self-consistent hydrodynamic simulations of such systems, which can be prime sources for multimessenger astronomy. In particular tilted black-hole-disk systems lead to (i) black hole precession, (ii) disk precession and warping around the black hole, (iii) earlier saturation of the Papaloizou-Pringle instability compared to aligned/antialigned systems, although with a shorter mode growth time scale, (iv) acquisition of a small black-hole kick velocity, (v) significant gravitational-wave emission via various modes beyond, but as strong as, the typical (2,2) mode, and (vi) the possibility of a broad alignment of the angular momentum of the disk with the black hole spin. This alignment is not related to the Bardeen-Petterson effect and resembles a solid body rotation. Our simulations suggest that any electromagnetic luminosity from our models may power relativistic jets, such as those characterizing short gamma-ray bursts. Depending on the black-hole-disk system scale the gravitational waves may be detected by LIGO/Virgo, LISA and/or other laser interferometers.

I. INTRODUCTION

Black holes (BHs) immersed in gaseous environments are ubiquitous in the Universe. Black hole disks (BHDs) appear on a great variety of scales, reflecting their diverse birth channels and sites. From the core collapse of massive stars [1,2] and the cores of active galactic nuclei [3–5], to asymmetric supernova explosions in binary systems [6], and the merger of compact binaries where at least one of the companions is not a BH, BHDs may be formed and serve as prime candidates for multimessenger astronomy.

The magnitude of the spin of the BH, as well as its orientation relative to the fluid flow, can have large effects, as in the existence and geometry of a relativistic plasma jet (see e.g. Ref. [7]). This jet, which can be powered either by magnetic fields threading the event horizon and extracting rotational energy from the BH [8], or from the accretion flow [9], can precess when misalignment between the BH and disk angular momentum arises [7,10,11]. Such misalignment is expected to be a common phenomenon [12] both in active galactic nuclei as well as in BH x-ray

binaries [6,10,11,13–17]. Even in the recent observation of M87 by the Event Horizon Telescope [18] misalignment could not be excluded [19,20].

Tilted BHDs are also the outcome of stellar-mass compact object collisions when their individual spins are not aligned with the orbital angular momentum [21–25]. Population synthesis studies suggest that in approximately half of the BH–neutron star binaries the angle between the orbital angular momentum and the BH spin is larger than 45° [26]. Such systems will yield misaligned BHDs which in turn will affect the existence and the properties of an electromagnetic counterpart, such as a short gamma-ray burst or a kilonova.

Central to the analysis of a tilted BHD is the so-called Lense-Thirring (LT) precession [27], a gravitomagnetic (GM) effect, according to which frame dragging produced by the rotating and tilted BH causes precession of a test ring with angular velocity $\Omega_{\rm GM-ring} \approx 2GJ_{\rm bh}/(c^2 r^3)$, where $J_{\rm bh}$ is the BH angular momentum, and r is the ring radius. In the presence of viscosity (for example, created by a magnetic field) the cumulative effect of LT precession and internal disk viscosity torques, is the alignment of the angular momenta of the BH and the disk, a phenomenon

*[*]tsokaros@illinois.edu

104010-1

known as the Bardeen-Petterson (BP) effect [28]. BP alignment typically occurs when the scale height of the accretion disk is substantially smaller than the viscosity parameter α [4], e.g. when $H/R \ll \alpha$ [28–30]. Due to the rapid fall-off behavior of the LT angular velocity, this alignment only affects the inner parts of the disk, within the so-called BP radius, while the outer parts keep their initial orientation. The GM field will make the BH precess around the disk's rotation axis. This effect has been invoked to explain the precession of jets in tidal disruption events (where a star is tidally disrupted by a supermassive BH) [31]. Even in the absence of a jet, the precession of such disks may have observable consequences. While disk precession has been invoked to explain the quasiperiodic oscillations [32] observed in the x-ray brightness of a number of neutron star and BH x-ray binaries [33–36], the BP alignment may prevent disks from precessing and producing such oscillations [37]. On the other hand BP alignment may be responsible for the growth and evolution of BHs [38].

In general, BHD systems (tilted or not) are subject to various instabilities that can lead to significant accretion and ablate away the disk. One such instability is the so-called dynamical runaway instability [39] where the overflow of a potential surface (similar to the Roche lobe) by the disk matter will lead to a cascading instability and the final consumption of the disk by the BH [40–42]. In binary mergers where a BHD is the final remnant, it was found [43,44] that the axisymmetric runaway instability is of limited importance due to the power-law dependence of the specific angular momentum profile of the disk [41]. Therefore its influence in the formation of ultrarelativistic jets is probably negligible [45–48].

A less dramatic instability was discovered by Papaloizou and Pringle [49] that transports angular momentum outwards and leads to the formation of a one-arm instability, the so-called Papaloizou-Pringle instability (PPI). Using perturbation theory, the authors found a quartic algebraic equation for the angular velocity of the perturbation mode whose solutions contain two stable modes (real solutions) and two unstable ones (imaginary solutions). These wave perturbations depend on the inner and outer radii of the disk [50,51] and highlight the importance of these boundaries in the development of the PPI. The instability manifests itself when a wave that is traveling backwards relative to the fluid at the inner edge exchanges energy and angular momentum with a wave that is traveling forwards relative to the fluid at the outer edge. Angular momentum is transferred outwards, making the wave at the outer edge that has positive angular momentum grow in amplitude while the one at the inner edge that has negative angular momentum also grow in amplitude, since it is losing angular momentum [52–61]. A similar mechanism in rotating stars leads to the Chandrasekhar-Friedmann-Schutz instability [62–64] which is induced

by gravitational radiation. The PPI, which was originally found in constant specific angular momentum disks, can also be developed in BHDs with a nonconstant specific angular momentum (ℓ) profile [52]. Newtonian analysis finds disks with $\ell \sim r^q$ where $q < 2 - \sqrt{3} = 0.266$ to be unstable, where the critical exponent q could be even smaller, i.e. $q \sim 0.25$ [53]. In general the growth of the nonaxisymmetric instability is more efficient for a smaller exponent q [51,53]. Accretion onto the BH has a stabilizing effect on the PPI since the waves at the inner boundary are disturbed [55,58,65]. This is especially true for wide disks, while in more slender ones the PPI seems to be less affected [66].

The first full general-relativistic simulations of a tilted thick disk onto a Kerr BH [67] have demonstrated that LT precession results in a torque that tends to twist and warp the disk, similar to Newtonian studies [68]. The authors found that this precession depends primarily on the sound speed in the disk. For disks where in their bulk the LT time scale is less than the azimuthal sound crossing time, the disk undergoes differential precession out to a transition radius. On the other hand when the LT time scale is greater than the azimuthal sound crossing time, the disk undergoes near rigid-body precession after a short initial period of differential precession. Another interesting finding in Ref. [67] was the tendency for these disks to align toward the equatorial plane of the BH, despite the lack of viscous angular momentum transport. According to the authors this alignment between the angular momentum of the disk and the BH spin was facilitated by the preferential accretion of highly tilted disk material that resulted in the depletion of the misaligned disk angular momentum. Since the authors considered disks with masses much smaller than the BH (test-fluid limit) the spin of the BH was unaffected. Such kind of purely hydrodynamical alignment has also been found in BH–neutron star simulations [23], where the alignment time scale was of the same order as the disk precession time scale. The authors speculated that this BP-like behavior is induced by a purely hydrodynamical mechanism, such as angular momentum redistribution due to a nonaxisymmetric shock wave excited in the disk.[1]

The assumption that the mass of the disk is negligible in comparison with the mass of the central BH may not always be valid. Some isolated or binary BHs detectable by LISA may find themselves immersed in extended disks with masses comparable or greater than the BHs

---

[1]Notice that in the numerical simulations of Ref. [69] using a post-Newtonian description of the central potential and an artificial viscosity, the BP picture of an aligned inner disk occurred only at low inclinations and only when Einstein precession was not accounted for. In high-resolution calculations with the Einstein precession included, the authors found steady-state oscillations in the disk tilt, as well as the breaking of the disks that are relatively thin and highly misaligned to the BH spin [30,68,70–72].

themselves. This may be particularly true of stellar-mass BHs in active galactic nuclei and quasars or supermassive BHs in extended disks formed in nascent or merging galactic nuclei. The gravitational pull of the disk on the binary can be important in such cases, the accretion rate from the inner disk radius can be high and even super-Eddington, orbital and spin precession as well as spin flipping in the case of misaligned disks is a possibility, and density perturbations in the disk can arise from instabilities. Alternative scenarios for the formation of massive BHDs include the collapse of rapidly rotating, supermassive stars or the merger of binary stellar systems (such as a neutron star–white dwarf binary) with significant asymmetry in their mass or spin. In binaries the mass of the disk depends on how far the secondary compact object being disrupted is from the BH [73]. If tidal disruption happens far from the innermost stable circular orbit (ISCO) of the BH, then a disk with a large mass is produced. On the other hand, small-mass disks (or even essentially no disk at all) are produced when tidal disruption happens close to the ISCO of the BH (or inside it). This crucial distance that controls the importance of self-gravitation for the disk depends on the mass ratio of the binary, the compactness of the primary and the BH spin. The mass of the disk increases with increasing BH spin (since the ISCO decreases with increasing spin) and decreases with increasing BH mass (the ISCO increases with increasing BH mass) [43,74].

Only by including self-gravity in full general relativity and tracking the nonaxisymmetric perturbations that self-gravity may trigger can gravitational waves from the disk be calculated reliably. Such perturbations and gravitational waves can be detected by LISA and other instruments [75–80]. Also, disk self-gravity must be incorporated to determine the astrophysical consequences of BH precession, which may, for example, trigger X-shaped radio galaxies [81–83].

General-relativistic studies of self-gravitating BHDs have been performed in a number of works [42,75–79,84,85] and the roles of the runaway instability, as well as the PPI, have been elucidated. Although most of the BHDs will not develop the runaway instability (e.g. Refs. [43,75,76,84]), it cannot be excluded when more favorable circumstances are present [42] (e.g. disks that fill their Roche lobes). Regarding the PPI, it was found that, as in Newtonian gravity, self-gravitating BHDs are subject to an $m = 1$ nonaxisymmetric mode growth under a wide range of conditions.[2] In Ref. [84] it was shown explicitly that the $m = 1$ PPI mode is accompanied by an outspiraling motion of the BH, which further amplifies the one-arm instability. More massive tori and a constant specific

angular momentum profile favor the appearance of the PPI, in contrast with less massive disks and/or a non-constant ℓ profile, for which the disk may even be PP stable [76]. In addition since the nonaxisymmetric structure survives long after the saturation of the PPI, these systems can be promising sources for coincident detections of electromagnetic and gravitational waves similar to GW170817. The above works focused on tori around nonspinning BHs and were later extended to BHDs around spinning BHs in [77,79,85]. In Ref. [79] it was speculated that the accretion rate in PPI unstable disks may be used to measure the BH spin. It was found that systems of ∼10 $M_\odot$—relevant for for BH–neutron star mergers—will be detectable by the Cosmic Explorer out to ∼300 Mpc, while DECIGO (LISA) will be able to detect systems of ∼1000 $M_\odot (10^5 M_\odot)$. The latter are relevant for disks forming in collapsing, supermassive stars out to a cosmological redshift of $z \sim 5 (z \sim 1)$. In Ref. [85] an alternative scenario for the event GW190521 was put forward. In particular it was conjectured that GW190521 may not represent the merger of binary BHs, but instead the stellar collapse of a very massive star, leading temporarily to a BH of mass ∼50 $M_\odot$ and a massive disk of several tens of solar masses that is dynamically unstable to the PPI.

The first general-relativistic simulations where the spin of the BH is tilted with respect to the angular momentum of the disk were performed in Refs. [77,78], albeit starting from artificial initial values. In particular the authors first computed models of self-gravitating, massive tori around nonrotating BHs [91], and then replaced the resulting spacetime with a tilted Kerr metric in quasi-isotropic coordinates, while retaining the hydrodynamical profile. Notwithstanding these initial conditions the authors performed a thorough investigation of the twist (precession) and the tilt (inclination) of the disk, finding that for BHD mass ratios of ≳4% the assumption of using a fixed background spacetime is unjustified. The authors observed significant precession and nutation of the tilted BH as a result of the disk evolution, which cannot be accounted for in fixed spacetime simulations. The LT torque that the BH exerts on the disk forces the disk to precess as a solid body which in turn leads to BH precession. The simulations of Refs. [77,78] showed the universal character of the PPI with regards to initial spin magnitudes, tilt angles, and disk angular momentum profiles.

In this work we extend previous studies of self-gravitating BHDs in two ways. For the first time we perform general-relativistic simulations of tilted BHDs starting from *self-consistent* initial values. The tilted BHD models are solutions of the full (i.e. including the conformal metric) general-relativistic initial value problem as described in Ref. [92]. Second, we extend the parameter space by evolving disks around *rapidly spinning* BHs (aligned, antialigned and tilted with respect to the disk angular momentum) having dimensionless spins up to 0.97. We find that although

---

[2]Note that early studies in Newtonian gravity [86–90] have shown that self-gravity inhibits the PPI for all angular momentum profiles, while new kinds of nonaxisymmetric instabilities arise. These include the I-mode ("intermediate") that leads to fission, and the J-mode (Jeans instability) that leads to fragmentation.

TABLE I. The initial BHD models. The angular momentum of the disks is along the z axis. Columns are the model name, the magnitude of the dimensionless BH spin $\chi = J_{bh}/M_{bh}^2$, the angles of the spin angular momentum in spherical coordinates (θ_s, ϕ_s), the inner specific angular momentum ℓ_{in}, the inner edge of the disk r_{in}, the maximum density coordinate r_c, the outer edge of the disk r_{out}, the rest mass of the disk M_0, the ADM mass M, the period of the maximum density point of the disk P_c, the dynamical time $t_d \sim 1/\sqrt{\rho_{max}}$, and the precession angular velocity P_{GM} of the BH as calculated in Sec. II A. Here M_{bh} is the mass of the BH. Center dots denote "not applicable.".

Model	χ	(θ_s, ϕ_s)	ℓ_{in}/M_{bh}	r_{in}/M_{bh}	r_c/M_{bh}	r_{out}/M_{bh}	M_0/M_{bh}	M/M_{bh}	P_c/M_{bh}	t_d/M_{bh}	P_{GM}/P_c
A1	0.966	$(0°, 0°)$	4.63	10	17.3	49.4	0.259	1.273	462	297	$\cdots$
A2	0.957	$(45°, 0°)$	4.60	10	17.3	49.4	0.156	1.167	435	371	60
A3	0.968	$(90°, 0°)$	4.85	10	17.9	51.1	0.280	1.298	455	290	35
A4	0.963	$(180°, 0°)$	5.13	10	20.0	57.3	0.242	1.256	520	364	$\cdots$

the saturation of the PPI appears significantly earlier for tilted BHDs than those with aligned/antialigned spins, due to the inherent initial nonaxisymmetry, their growth rate is smaller. The maximum density in the disk can increase by orders of magnitude, while the disk precesses and warps around the BH. The BH itself also precesses and its spin can increase or decrease depending on the initial configuration. In one case where the initial BH spin is tilted at $45°$ with respect to the angular momentum of the disk the BH is spun up to a maximal value, beyond which we cannot continue our simulation. In another case where the initial BH spin is tilted by $90°$ accretion spun the BH down. By computing the precession time scales we confirm their agreement with post-Newtonian estimates. The precessing BHDs are responsible for copious gravitational-wave emission in multiple modes, which we compute. In general the gravitational-wave strain appears to be an order of magnitude larger than previous calculations [76,77,79,85] with a diverse spectrum. Although our simulations do not include magnetic fields, estimation of the effective turbulent magnetic viscous time scale shows that it is much longer than the dynamical time scale of the one-arm instability. Therefore we expect these BHDs to be prominent sources of gravitational waves and Poynting electromagnetic radiation (in the presence of magnetic fields) and thus excellent sources for multimessenger astronomy.

In this paper, spacetime indices are greek, spatial indices latin, and we employ geometric units in which $G = c = M_\odot = 1$, unless stated otherwise.

II. INITIAL DATA

The initial models of the BHDs considered in this work, models A1–A4 in Table I, have been constructed using the COCAL code and the method described in Ref. [92]. In particular we solve the full initial value Einstein equations by assuming that the conformal three-dimensional metric is decomposed as $\tilde{\gamma}_{ij} := f_{ij} + h_{ij}$, where f_{ij} is the flat metric and h_{ij} are the nonflat contributions. The metric on the 3-geometry γ_{ij} is related to the conformal metric through $\gamma_{ij} = \psi^4 \tilde{\gamma}_{ij}$. The nonflat contributions h_{ij} are computed

alongside the lapse α, shift β^i, and the conformal factor ψ, assuming $\det(\tilde{\gamma}_{ij}) = \det(f_{ij})$. One of the new characteristics of this method is the decomposition of the conformal trace-free part of the extrinsic curvature as

$$\tilde{A}_{ij} = \tilde{A}_{ij}^{KS} + \tilde{\sigma}(\tilde{\mathbb{L}}\,\tilde{W})_{ij}, \tag{1}$$

where $\tilde{A}_{ij}^{KS}$ is the conformal Kerr-Schild trace-free part, $\tilde{W}_i$ is an unknown spatial vector, $\tilde{\sigma}$ is a scalar, and $\tilde{\mathbb{L}}$ is the conformal Killing operator: $(\tilde{\mathbb{L}}\,\tilde{W})_{ij} = \tilde{D}_i\tilde{W}_j + \tilde{D}_j\tilde{W}_i - \frac{2}{3}\tilde{\gamma}_{ij}\tilde{D}_k\tilde{W}^k$. Here $\tilde{D}_i$ is the covariant derivative with respect to the conformal metric $\tilde{\gamma}_{ij}$. It is assumed that $A_{ij} = \psi^4\tilde{A}_{ij}$ and $\tilde{\sigma} = 1/(2\alpha)$. As explained in Ref. [92], Eq. (1) with the appropriate boundary conditions for $\tilde{W}_i$ yields a convergent solution for the potentials h_{ij}, which in addition, can be horizon penetrating. The price paid for this additional decomposition of the extrinsic curvature is an extra three elliptic equations for the potentials $\tilde{W}_i$. For the slicing we assume Kerr-Schild coordinates with $K = K_{KS}$ under the gauge $\mathring{D}_i h^{ij} = \mathring{D}_i h_{KS}^{ij}$, with h_{KS}^{ij} being the exact Kerr-Schild potentials, and $\mathring{D}_i$ the covariant derivative with respect to the flat metric f_{ab}. We set $\partial_t\tilde{\gamma}_{ij} = \partial_t\tilde{A}_{ij} = \partial_t K = 0$.

For the Euler equations we assume stationarity and axisymmetry [92], which is a reasonable assumption whenever the disk is far away from the tilted BH. The density profiles along the x axis for our models are plotted in the top panel of Fig. 1. The disk is described by a $\Gamma = 4/3$ polytropic equation of state,[3] having constant specific angular momentum $\ell = -u_\phi/u_t$. Note that there exist other diagnostics for the specific angular momentum, such as $j = u_t u^\phi = \ell/(1 - \Omega\ell)$, as well as hu_ϕ. Here h is the specific enthalpy, u_ϕ is the azimuthal component of the 4-velocity, and $\Omega = u^\phi/u^t$ is the angular velocity of the fluid. The three diagnostics are plotted in the bottom panel

---

[3]This choice is appropriate for a thermal radiation-dominated gas, which might be found around a supermassive BH, but is not the optimal choice for BH–neutron star binaries.
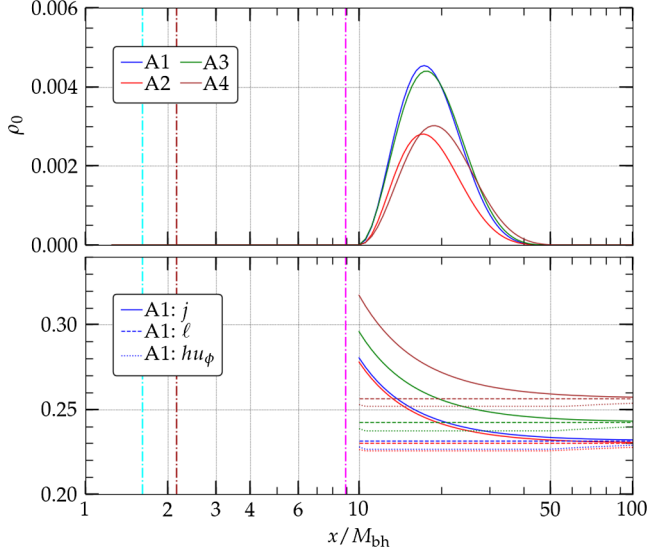
FIG. 1. Top panel: initial rest-mass density distribution for the four models evolved. Bottom panel: specific angular momentum of the BHD model A1. Solid lines correspond to j, dashed lines to ℓ and dotted lines to hu_ϕ. The vertical dash-dotted lines correspond to the event horizon (cyan), the marginally stable radius for the prograde orbit (brown), and the marginally stable radius for the retrograde orbit (magenta) around a BH whose dimensionless spin is $\chi = 0.95$.

of Fig. 1 for case A1 while similar behavior can be found for cases A2–A4. Our disk models have constant ℓ and hu_ϕ.

For the numerical solution of the Poisson-type of equations we use the Komatsu-Eriguchi-Hachisu method for BHs, which was first developed in Ref. [93]. The self-gravitating BHD is calculated as follows. (i) First we calculate a massless disk [94,95] around a tilted, spinning BH whose mass is m and dimensionless spin is $a/m = 0.95$. We call m the BH bare mass. (ii) Using as
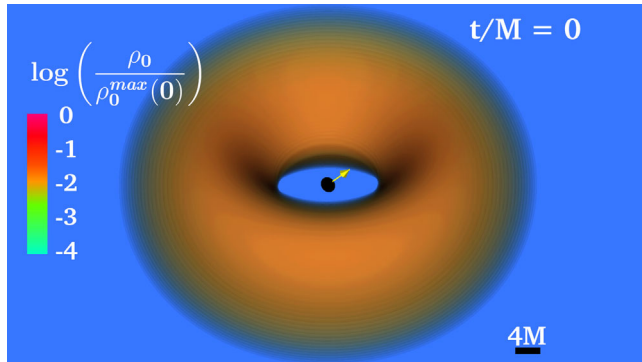
initial data the solution obtained in step (i) we iterate over the Einstein and Euler equations to compute a self-gravitating disk of a given maximum rest-mass density. (iii) By increasing the maximum density of the disk and repeating step (ii) we compute a sequence of BHDs whose disk mass is growing. For each solution the angular momentum of the BH J_{bh} is calculated through the isolated horizon formalism [96,97]. Using the apparent horizon finder described in Ref. [93] we calculate the mass of the BH M_{bh} [98], and its dimensionless spin $\chi = J_{bh}/M_{bh}^2$. In Fig. 2 a full three-dimensional rendering of the BHD model A2 is shown. The yellow arrow depicts the spin of the BH, which is tilted at 45° with respect to the z axis. The latter coincides with the axis of rotation of the disk. The apparent horizon is denoted by a black spheroid which is similarly tilted. Models A1, A3, and A4 have similar disk structure, differing mainly in the tilt angle of the BH.

A. Precession frequencies

The relevant post-Newtonian (PN) theory for understanding a massive disk around a tilted BH is summarized in Ref. [99], which we closely follow in the analysis below. In particular we assume a massive thin disk confined in the x-y plane having angular momentum $\mathbf{J}_d$ along the z axis, and whose inner radius is b_{in} while its outer radius is b_{out} (see Fig. 3). The disk rotates about a BH having angular momentum $\mathbf{J}_{bh}$ tilted with respect to $\mathbf{J}_d$. We further assume that the disk lies outside the BP radius so that it is not driven down to the hole's equatorial plane (perpendicular to $\mathbf{J}_{bh}$). In our simulations there is no viscosity, so in principle there

FIG. 2. Three-dimensional rendering of BHD model A2 at $t = 0$. The direction of the BH spin tilted at 45° with respect to the z axis (axis of the orbital angular momentum of the disk) is shown by the yellow arrow. The black spheroidal region denotes the apparent horizon.
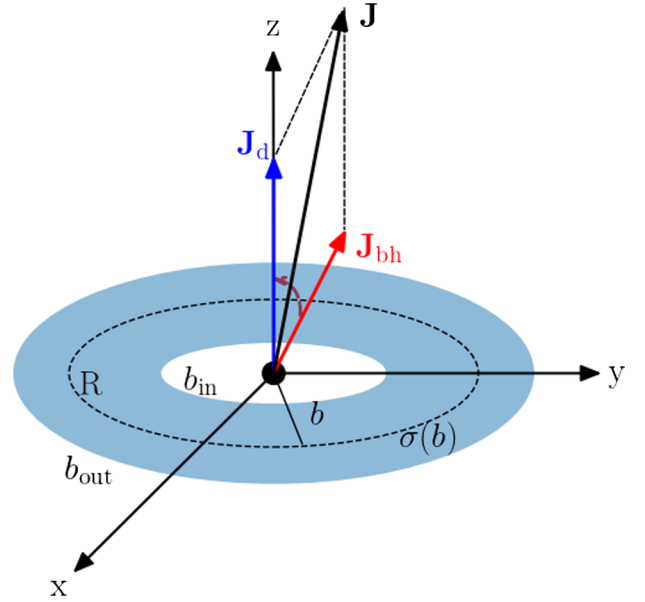

FIG. 3. A thin massive disk in the x-y plane with angular momentum $\mathbf{J}_d$ along the z axis rotates around a tilted spinning BH with angular momentum $\mathbf{J}_{bh}$. Both of them undergo GM precession about the total angular momentum $\mathbf{J}$.

is no such accretion and no BP effect.[4] Now we imagine that the thin disk is composed of massive rings, each one of them having a mass dM_R, and radius b. The ring's GM field will make the BH precess around the disk's rotation axis $d\mathbf{J}_{bh}/dt = \mathbf{\Omega}_{GM} \times \mathbf{J}_{bh}$ where $\Omega_{GM} = 2J_R/b^3$ and J_R is the angular momentum of the ring. Generalizing to the disk of Fig. 3 we can write

$$d\Omega_{GM} = \frac{2}{b^3} dJ_R(b). \qquad (2)$$

If $\sigma(b)$ is the surface gas density and $\omega(b)$ is the angular velocity of the ring, we have

$$dJ_R(b) = \omega(b)b^2 dM_R = \omega(b)b^2(\sigma(b)2\pi b db), \quad (3)$$

where

$$\sigma(b) = \int_{-h(b)}^{h(b)} \rho_0(b,z)dz, \quad \omega(b) = \int_{-h(b)}^{h(b)} \Omega(b,z)dz, \quad (4)$$

are calculated as quadratures over the disk height $h(b)$ at the particular radius b. In Eq. (4) $\rho_0(b, z)$ is the rest-mass density of our three-dimensional disks, and $\Omega(b, z)$ is their angular velocity profile. Note that although in Newtonian gravity for a barotropic fluid the angular velocity of a stationary disk depends only on the distance from the axis of rotation (Poincaré-Wavre [101]), in general relativity the surfaces of constant Ω (von Zeipel's cylinders [100]) have cylindrical topology, and therefore they depend not only on the distance from the rotation axis but also on the distance from the equatorial plane [102,103].

From Eqs. (2)–(4) the GM precession angular velocity of the BH will be

$$\Omega_{GM} = \int_{b_{in}}^{b_{out}} 4\pi\omega(b)\sigma(b)db, \qquad (5)$$

where b_{in} and b_{out} are the radial boundaries of the disk. Inserting the density and angular velocity of our tilted self-gravitating disk models A2 and A3 into Eqs. (4)–(5), we can compute Ω_{GM}. These theoretical PN estimates are reported in the last column of Table I in terms of the GM precession period $P_{GM} = 2\pi/\Omega_{GM}$.

Note that a ring of mass M_R rotating with Keplerian angular velocity around a BH of mass M_{bh} at a radius b_R will be subject to GM precession with

---

[4]As we discussed in the Introduction, in Ref. [23] the authors found such alignment in pure hydrodynamical simulations. In any case, even if numerical viscosity is present we assume that the bulk of the mass and angular momentum of the ambient disk remains largely intact (apart from precession).

$$M\Omega_{GM} = 2\left(\frac{M}{b_R}\right)^{5/2}\left(\frac{M_{bh}}{M}\right)^{1/2}\left(\frac{M_R}{M}\right), \qquad (6)$$

where M is the Arnowitt-Deser-Misner (ADM) mass of the system. For our models {A2, A3} Eq. (6) yields $P_{GM}/P_c = \{54, 31\}$ in rough agreement with the values shown in Table I. This shows that despite the constant specific angular momentum our self-gravitating disks are effectively close to the Keplerian test-ring model.

Not only does the disk makes the BH to precess: conservation of the total angular momentum $\mathbf{J} = \mathbf{J}_{bh} + \mathbf{J}_d$ implies that the BH will make the disk to precess, i.e.,

$$\frac{d\mathbf{J}_d}{dt} = \left(\frac{2\mathbf{J}_{bh}}{b^3}\right) \times \mathbf{J}_d. \qquad (7)$$

The precession frequency of the disk $\Omega_{GM-disk}$ is related to the precession frequency of the BH Ω_{GM} as

$$\Omega_{GM-disk} = \Omega_{GM}\frac{J_{bh}}{J_d}. \qquad (8)$$

For models A2 and A3 we find that $P_{GM}/P_{GM-disk}$ is of order 1.0 implying that the spin of the BH will precess at the same time scale as the warping of the disk.

As a final note we mention that the disk's tidal field will also exert a torque on the BH that leads to tidally torqued precession with angular velocity [99]

$$\Omega_T = \frac{3aM_R}{2b_R^3}\cos\theta_s. \qquad (9)$$

For model A2 we find $P_T/P_{GM} \approx 8$ using b_R as the radius of the maximum density. On the other hand we can perform an analysis similar to the GM frequency and write $d\Omega_T = 3adM_R\cos\theta_s/(2b^3)$, with $dM_R = \sigma(b)2\pi b db$. Integrating as in Eq. (5), we find $P_T/P_{GM} \approx 9$ in agreement with the cruder estimate above. Therefore the tidally torqued precession is secondary to the GM precession and needs very long evolutions to be probed.

III. EVOLUTIONS

The models A1–A4 of self-gravitating BHDs are evolved using the Illinois GRMHD moving-mesh-refinement code that employs the Baumgarte-Shapiro-Shibata-Nakamura (BSSN) formulation of the Einstein equations [104,105] to evolve the spacetime fields. Outgoing wavelike boundary conditions are applied to all BSSN variables, which are evolved using the equations of motion (9)–(13) in Ref. [106], along with the $1 + \log$ time slicing for the lapse α, and the "Gamma-freezing" condition for the shift β^i, cast in first-order form [see Eq. (2)–(4) in Ref. [106]]. Time integration is performed via the method of lines using a fourth-order accurate Runge-Kutta integration scheme with a Courant-Friedrichs-Lewy factor set to 0.36. Spatial

derivatives are computed with fourth-order, centered finite differences, except on shift advection terms, where we employ fourth-order upwind differencing. We use the Carpet infrastructure [107,108] to implement moving-box adaptive mesh refinement, and add fifth-order Kreiss-Oliger dissipation [109] to spacetime and gauge field variables. For numerical stability, we set the damping parameter η appearing in the shift condition to $\eta \approx 26.6/M$. For further stability we modify the equation of motion of the conformal factor ϕ by adding a constraint-damping term [see Eq. (19) in Ref. [110]] which damps the Hamiltonian constraint. We set the constraint-damping parameter to $c_H = 0.08$ (see also Ref. [111]).

High-resolution, shock-capturing methods [112,113] are used for the equations of hydrodynamics, which are written in conservative form. The primitive, hydrodynamic matter variables are the rest-mass density, ρ_0, the pressure P and the coordinate 3-velocity $v^i = u^i/u^0$. The stress-energy tensor is $T_{\alpha\beta} = \rho_0 h u_\alpha u_\beta + P g_{\alpha\beta}$. For the equation of state we use the ideal-gas Γ law $P = (\Gamma - 1)\rho_0\epsilon$ with $\Gamma = 4/3$, and ϵ is the specific internal energy. The grid hierarchy used in our simulations is summarized in Table II. It consists of a set of 13 nested mesh-refinement boxes centered on the BH apparent horizon. The computational domain is $[-4000M_{\rm bh}, 4000M_{\rm bh}]^3$. The half-side length of the finest box has $\Delta x_{\rm min} = 50M_{\rm bh}/2^{12} = 0.0122M_{\rm bh}$. Note that the ADM mass is $M \approx 1.2$–$1.3M_{\rm bh}$ depending on the model. In our simulations we do not assume any symmetry. The extremely high resolution used is necessary in order to accurately capture the dynamics of the highly spinning BHs.

A. Global structure

The overall evolution of models A1–A4 can be seen in Figs. 4 and 5. At $t = 0$ (left column of Fig. 4) the disks have very similar geometries (see also Fig. 1) while the BHs have the same mass and similar spin magnitudes. Thus the main difference in our cases is the BH tilt angle, which results in distinct behaviors for the four models. Note that in Figs. 4 and 5 the magnitude of the BH spin vector is not to scale. Also the shrinkage of the BH and the disk sizes in the right column of Fig. 4, and the left column of Fig. 5 is due to gauge effects arising from differences between the initial data and the evolution gauge choices. In the right column of Fig. 4 we depict a meridional cut at the final moment in our evolutions. For the aligned case (top row) the BH preserves its spin orientation and magnitude and the disk retains its broad characteristics. The one-arm instability fully develops, but the induced BH orbit remains bounded. On the other hand, the antialigned case (bottom row) after a certain time becomes largely unstable, with the disk losing its initial structure and exhibiting massive mass accretion. The BH acquires a kick velocity (keeps drifting away until the end of our simulations). Although the BH

spin orientation is preserved, its magnitude is significantly reduced due to accretion.

For the misaligned cases (second and third rows), we observe the combined effects of (i) BH precession, (ii) disk precession and warping around the BH, (iii) development of the PPI, (iv) acquisition of a small BH kick velocity, (v) significant gravitational-wave emission of various modes beyond the $\ell = 2$, $m = 2$ which are as strong as the (2,2) mode, and (vi) in the A3 case (90° initial tilt) an overall broad alignment of the disk with the BH spin (third row in Fig. 4, right column). This alignment is not associated with the BP effect, which requires a viscosity mechanism absent in our simulations. True BP alignment has only been observed in GRMHD simulations of very thin disks with scale heights below $H/R < 0.05$ (e.g. Ref. [114]). There has been no indication that BP alignment for thicker accretion disks is possible. That said, thicker accretion disks can, and do align as a whole, not just the inner disk [7,115,116]. In these cited GRMHD simulations this "global" mode happened on the viscous time of the disk and thus does not produce a steady-state solution as envisioned by BP. In our *hydrodynamical* simulations the disks have $H/R \sim 0.625$ and thus the flow is not susceptible to BP warps (at least initially). Similarly to Refs. [7,67,115,116] the possible alignment is global, i.e. the whole disk rotates like a solid body, instead of the local alignment of only the inner regions of the disk typical of the BP picture. In fact, from the third row, right column of Fig. 5, where the two streams onto the BH are apparent, we confirm that there is no such alignment in the inner regions of the disk. Our results are reminiscent of the behavior described in Refs. [67,115] and are referred to as "plunging streams." The additional complication in our case though is that the BH-disk spacetime is dynamical and responds to the motion of the disk. The alignment in case A3 happens on a shorter time scale than the effective viscous time scale reported in Sec. III D. As in Refs. [67,115] the plunging streams enter the BH above and below its symmetry plane from almost antipodal points due to strong differential precession and the nonspherical nature of the spacetime. For a Kerr BH (which is very close to the BHD spacetimes close to the horizon) orbital stability strongly depends on the inclination of the orbit, with the unstable region being larger for increasing inclination. Also the value of $r_{\rm ISCO}$ is larger for larger inclinations [115,117]. For the A3 case we observe the largest BH kick velocity which is ~ 2 km/s. For model A2 (45° initial tilt angle) we could not evolve beyond $t \approx 3133M$ because the BH was spun up to maximal spin. At that point both the BH and the disk experience a tilt by $\sim 45°$ with respect to their initial orientation, but in opposite directions (see second row, right column in Fig. 4) Similar to case A3 and Refs. [67,115], we observe two plunging streams in opposite directions entering the BH above and below its symmetry plane. The warping of the disk around the BH for

TABLE II. Grid parameters used for the evolution of the BHDs of Table I. The computational grid consists of a set of 13 nested refinement boxes centered on the BH apparent horizon. The step interval in the coarser level is $\Delta x_{max} = 50 M_{bh}$, while in the finer refinement level it is $\Delta x_{min} \approx 0.0122 M_{bh}$. Note that the ADM mass $M \approx 1.2$–$1.3 M_{bh}$ depending on the model.

$\{x, y, z\}_{min}$	$\{x, y, z\}_{max}$	Grid hierarchy (Box half-length)
$-4000 M_{bh}$	$4000 M_{bh}$	$\{0.5, 1.56, 3.12, 6.24, 12.48, 25, 50, 100, 200, 399, 799, 1597, 4000\} M_{bh}$
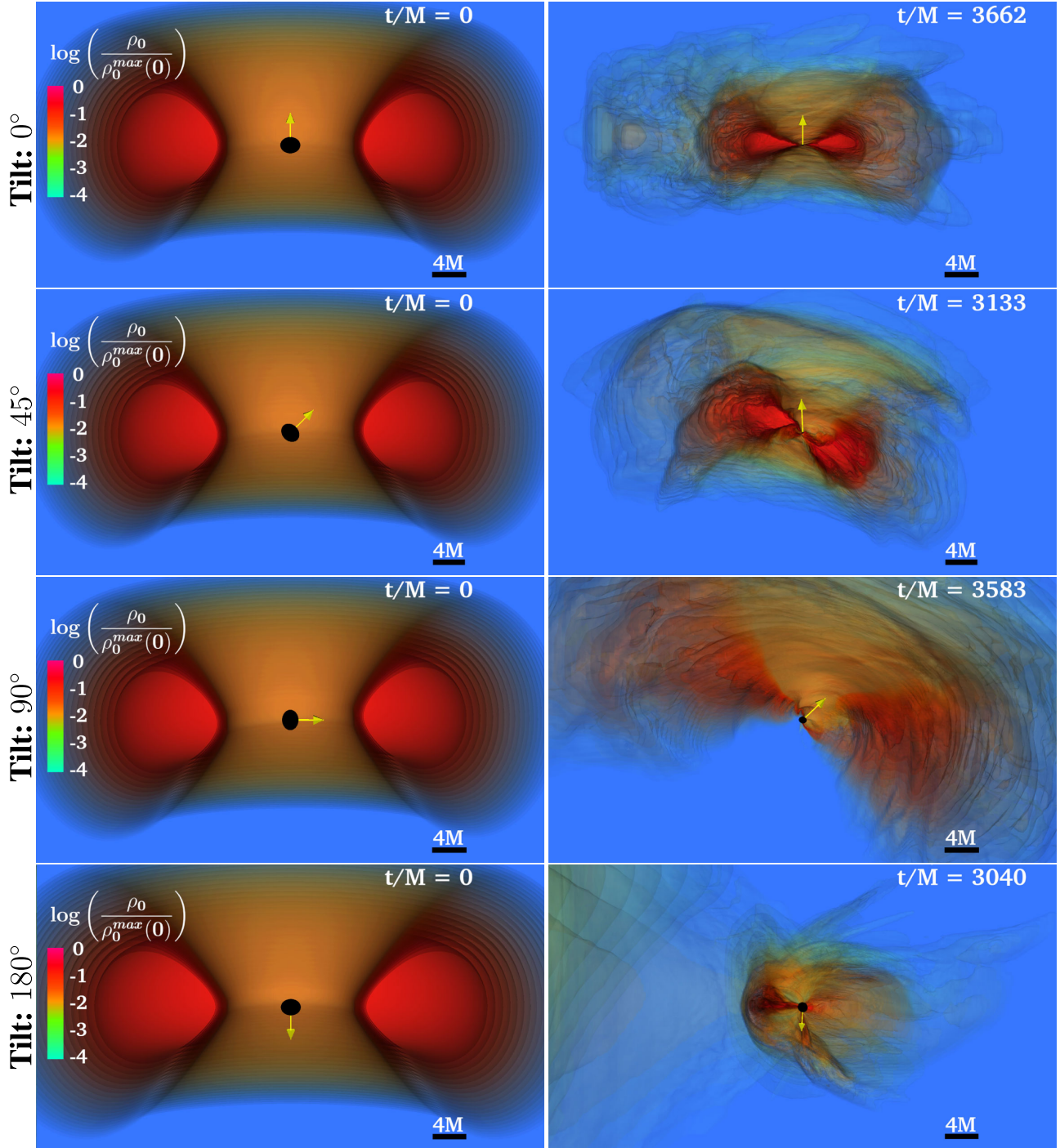
FIG. 4. Meridional cuts for the initial (left column) and final (right column) state of the rest-mass density for models A1 (first row), A2 (second row), A3 (third row), and A4 (fourth row). The direction of the BH spin is given by the yellow arrow. The black spheroidal regions denote the apparent horizon.
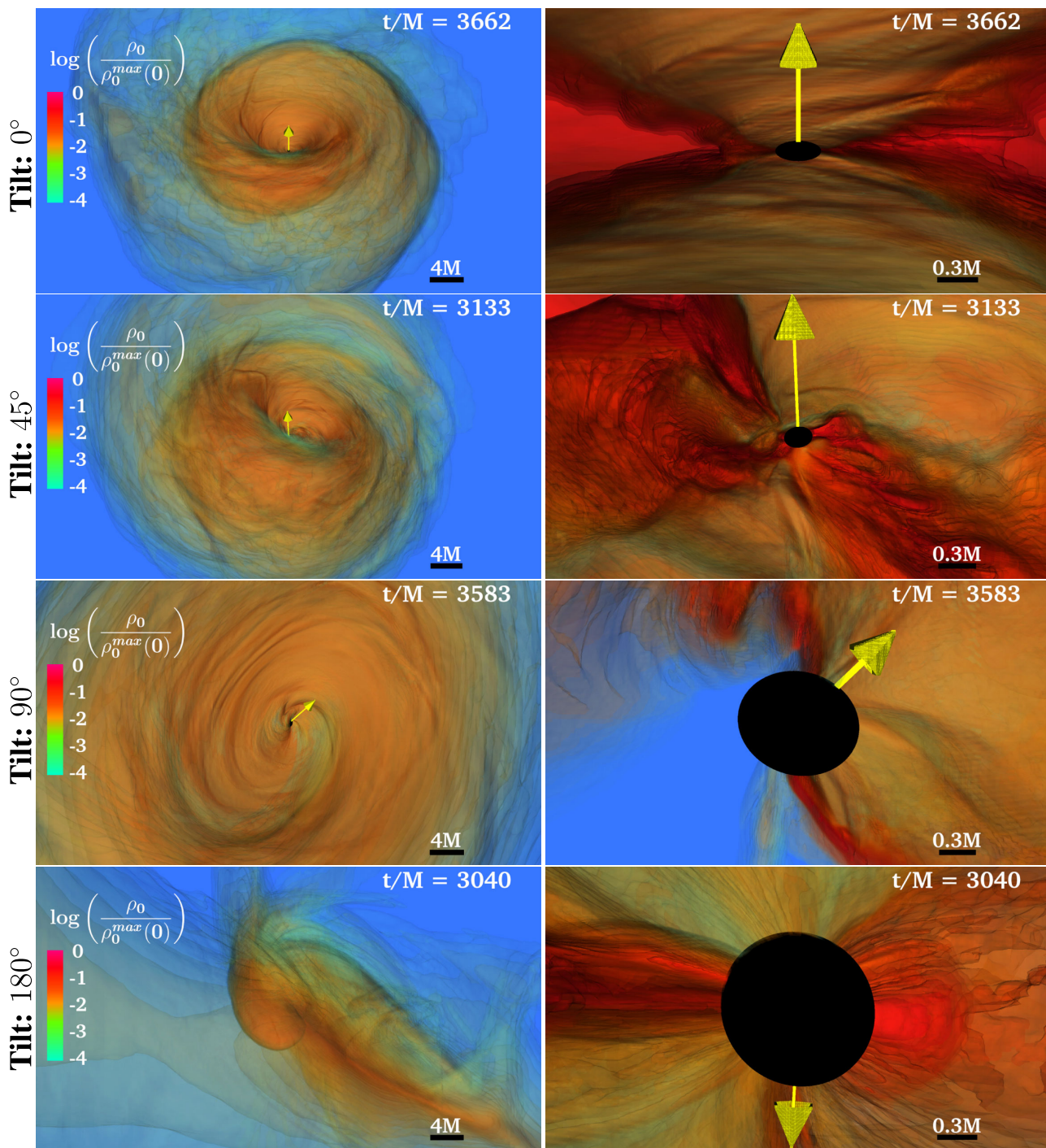
FIG. 5. The left column shows the full three-dimensional rendering of the disk rest-mass density at the final moment of our simulations. The right column zooms in near the BH at the same time as in the left column. The rest-mass densities are plotted for models A1 (first row), A2 (second row), A3 (third row) and A4 (fourth row). The direction of the BH spin is given by the yellow arrow. The black spheroidal regions denote the apparent horizon.

both cases A2 and A3 is significant (see second and third rows of Fig. 5).

B. Mode growth and angular momentum transport

According to previous studies, both Newtonian and general relativistic, we expect all our models to be dynamically unstable to the one-arm ($m = 1$) spiral-shape instability. In the general-relativistic simulations of Refs. [77,78,84] it was concluded that if the mass of the disk is larger than $\gtrsim 4\%$ of the mass of the BH a fixed background spacetime cannot fully capture the dynamics of the system. In particular in order to accurately describe the

dynamical gravitational interaction between a time-varying BH (in position, mass and spin), as well as a time-varying massive disk, simulations in a nonfixed background spacetime are necessary, as we perform here.

To quantify the growth of various unstable density modes we evaluate the parameters [79,118]

$$C_m = \int_{r>r_{ah}} \rho_0 u^t \sqrt{-g} e^{im\phi} d^3x, \qquad (10)$$

where g is the determinant of the spacetime metric and $\phi = \tan^{-1}(y/x)$ is the azimuthal angle. The volume integral is performed outside the apparent horizon of the BH and the mode amplitude is denoted by the normalized quantity C_m/C_0, where $C_0 = M_0$ is the rest mass of the disk. The pattern speed of an azimuthal mode m is defined as [119,120]

$$\Omega_{p,m} = \frac{1}{m}\frac{d\phi_m}{dt}, \qquad (11)$$

with the phase angle ϕ_m being

$$\phi_m = \tan^{-1}\left(\frac{\text{Im}(C_m)}{\text{Re}(C_m)}\right). \qquad (12)$$

In other words the pattern speed of any mode is proportional to the slope of the curve $\phi_m(t)$ with the proportionality constant being $1/m$.

As we discussed in the Introduction, the PPI manifests itself when a perturbation that is traveling backwards relative to the fluid at the inner edge, and therefore has $\Omega_{p,m} < \Omega$, exchanges energy and angular momentum with a perturbation that is traveling forwards relative to the fluid at the outer edge and therefore has $\Omega_{p,m} > \Omega$. The radius r_{cr} where the interaction happens is called the corotation radius and satisfies $\Omega_{p,m} = \Omega(r_{cr})$.

In Fig. 6 we plot the $m = 1$ (top panel) and $m = 2$ (bottom panel) mode growths for all cases: A1 (aligned, blue line), A2 (45° red line), A3 (90° green line), and A4 (180° brown line). The most prominent feature of this plot is the fact that for both modes, the $(C_m/C_0)(t = 0)$ values for the tilted cases (A2 and A3) are much larger than those for A1 and A4.[5] In fact for models A2 and A3 $(C_2/C_0)(t = 0) \sim O(10^{-2})$ is 10 to 100 times larger than $(C_1/C_0)(t = 0)$ and initially slightly decreases while the latter steadily grows in an exponential manner. When C_1/C_0 reaches values $\sim O(10^{-2})$ then the $m = 2$ mode grows in a similar manner. In other words the $m = 1$ mode drives the growth of the $m = 2$ mode, something that is also seen in the aligned and antialigned cases (A1 and A4).

_____

[5]For models A1 and A4, at $t = 0$ slight deviations from $C_m \equiv 0$, $m \geq 1$, are due to numerical error, as the disks are constructed to be strictly axisymmetric in spherical polar coordinates and then interpolated onto a Cartesian grid.
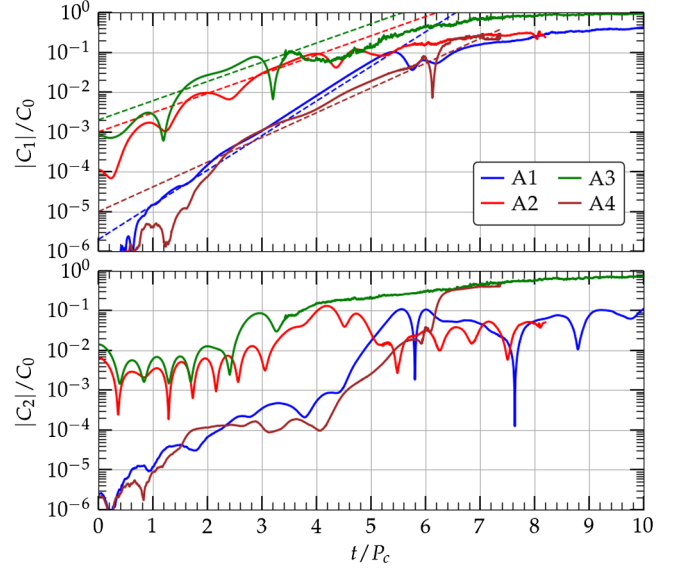

FIG. 6. Growth of the $m = 1$ (top panel) and the $m = 2$ (bottom panel) modes.

The fact that in the tilted cases at $t = 0$ the $m = 1$ mode amplitude is already nonzero and much larger than in the aligned or antialigned cases results in a smaller $m = 1$ growth time scale, as can be seen from the slope of the fitted dashed lines (in the top panel of Fig. 6). These time scales are reported in the second column of Table III and are in broad agreement with other studies [79,84]. If we denote the growth of the $m = 1$ mode as $e^{t/\tau}$, we find that $\tau/P_c = \{0.5, 0.9, 0.9, 0.7\}$ for cases A1–A4, confirming that the instability is indeed dynamical. The two tilted cases show almost identical growth time scales, even though the disk in case A3 has almost double the mass of the disk in case A2 while their radial extent is approximately the same. Note that in Refs. [76,80] it was found that more compact (or more massive) disks are more subject to the dynamical instability, and when $M_0/M_{bh} \gtrsim 0.6$ the growth time scale can be smaller than P_c. Our models show that time scales $\lesssim P_c$ are possible with even less massive disks with $M_0/M_{bh} \sim 0.16$. This result is not surprising [54] since our disk models have $\ell = \text{const}$ which makes them more prone to the development of the PPI than the models of Refs. [76,80], which have a nonconstant specific angular momentum profile. Given the fact that models A2 and A3

TABLE III. Mode growth, pattern speed, and corotating radius for the $m = 1$ mode.

| Model	$\text{Im}(\omega_1)/\Omega_c$	$\Omega_{p,1}/\Omega_c$	r_{cr}/r_c
A1	0.318	0.748	1.17
A2	0.177	0.748	1.17
A3	0.177	0.637	1.24
A4	0.227	0.812	1.12
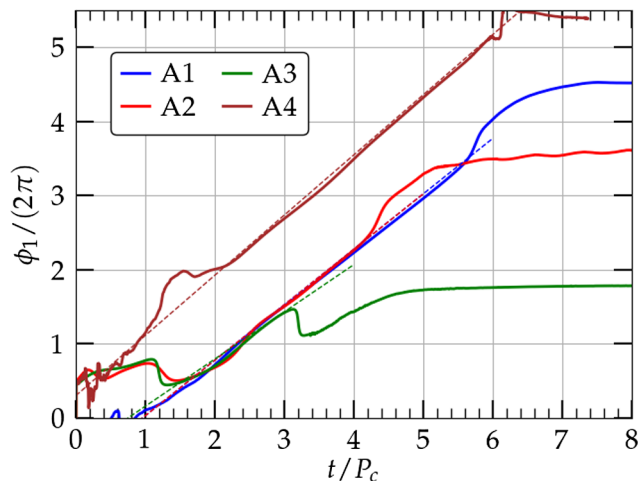
FIG. 7.   Phase angle ϕ_1 of the mode $m = 1$ for models A1–A4.

have the same spin magnitude we conclude that the spin tilt is crucial for the determination of the growth time scale and can be degenerate with the BH-to-disk mass ratio.

The phase angle of the $m = 1$ mode is shown in Fig. 7 and the slopes of the fitted dashed lines [Eq. (11)] provide the corresponding pattern velocities $\Omega_{p,1}$ that are quoted in Table III. From this figure one can easily read the time for the saturation of the PPI. In particular for case A1 it is $\approx 5.5 P_c$, for A2 it is $\approx 4 P_c$, for A3 it is $\approx 3 P_c$, and for A4 it is $\approx 6 P_c$. These values are in agreement with the top panel of Fig. 6 and show that the larger the tilt, the smaller the time span for the development of the nonaxisymmetric insta-bility. After this initial period, the mode growth saturates and the phase angle ϕ_1 asymptotes to a constant. Interestingly, the $m = 1$ pattern speed is almost identical for cases A1 and A2 despite the different spin orientations of the BHs, as well as the different BH-to-disk mass ratios. This may be related to the fact that those models have identical inner r_{in} and outer r_{out} boundaries, which play a crucial role for the explanation of the PPI [49,50,52,53].

Another critical component of the PPI is the corotation radius r_{cr} through which angular momentum is transferred outwards [49,53,54,58]. In Table III we report the ratio of the corotation radius to the radius of the maximum density for our models A1–A4. This ratio is close to unity, which is typical of the $m = 1$ PPI mode [77,78,84]. In terms of the total mass of the system the corotation radii are $r_{cr}/M = \{16, 17, 17, 17\}$. In order to confirm and better understand the development of the PPI in thick, tilted self-gravitating BHDs we plot in Fig. 8 the specific angular momentum $\ell = -u_\phi/u_t$ at three different instances for case A2. At one rotation period (left panel) the disk has essentially the angular momentum profile of the initial data i.e. $\ell = $ const. After three rotation periods (middle panel), when the PPI has been well developed, we see two characteristics: (i) a shock front located at approximately $r \sim 20M$, and (ii) the shock front separating the inner part ($r \lesssim 20M$) of the disk with angular momentum regions having values smaller than the initial angular momentum (white-blue areas) from the outer part ($r \gtrsim 20M$) of the disk with angular momentum regions having values larger than the initial angular momentum (green-yellow-red areas). Also, a spiral structure in the outer part starts to form. After six rotation periods (right panel), where the PPI is fully developed, this picture is even clearer and the characteristic spiral arm is apparent. This shows how the PPI can redistribute angular momentum by outward transport.

The growth of the one-arm instability results in a pseudobinary system consisting of the BH and the $m = 1$ "planet" that sets the BH in motion. In Fig. 9 we depict the trajectory of the BH in the equatorial (top panel) and meridional (bottom panel) planes. In all cases we notice the characteristic spiral trajectory resulting from the spiral motion of matter in the disk (see the left column of Figs. 5 and 8) and the conservation of the center of mass of the system. For case A1 the motion is planar (in the x-y plane) with larger radius of curvature in the beginning when the PPI develops and smaller at the end, when it has saturated.
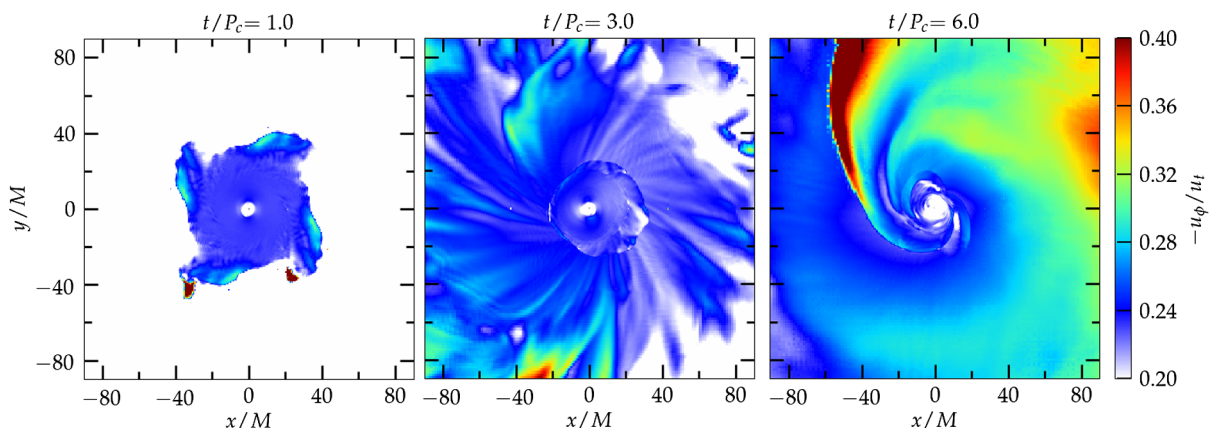
FIG. 8.   Snapshots at three different times of the specific angular momentum $\ell = -u_\phi/u_t$ for case A2. To convert to t/M multiply by 373 (see Table I).
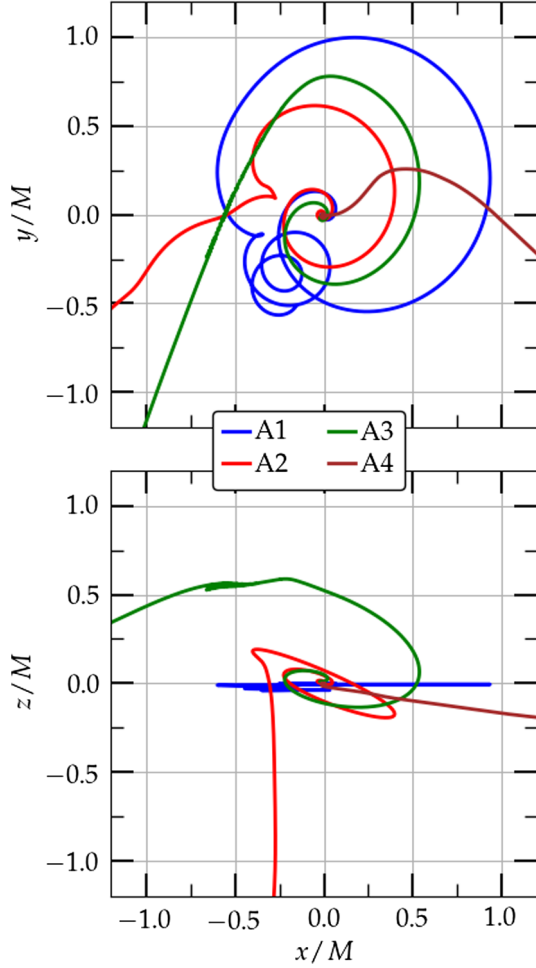
FIG. 9. BH trajectory in the x-y and x-z planes.

For the tilted cases A2 and A3 this motion is three dimensional, while for the antialigned case A4 we again have a three-dimensional motion due to the destabilization of the whole system after $\sim$ six rotation periods.[6] The evolution of A4 will be further described in the next section. The combined motion of the BH with the self-gravitating disk produces copious amounts of gravitational radiation, as we will discuss next.

C. Precession and gravitational waves

In the top panel of Fig. 10 we plot the evolution of the maximum density in the disk. The general trend shows the maximum density to be constant until approximately the end of the development of the PPI, at which point nonlinear growth sets in and can lead to an increase of $\rho_{0,\max}$ by orders of magnitude. Consistent with Figs. 6 and 7 we observe that the peak of $\rho_{0,\max}$ for case A1 occurs at $\sim 6P_c$ which coincides with the end of the linear growth of

---

[6]Note that the linear drift observed in the later part of the A2 and A3 orbits in Fig. 9 may be partly due to the BSSN formalism used in our simulations.
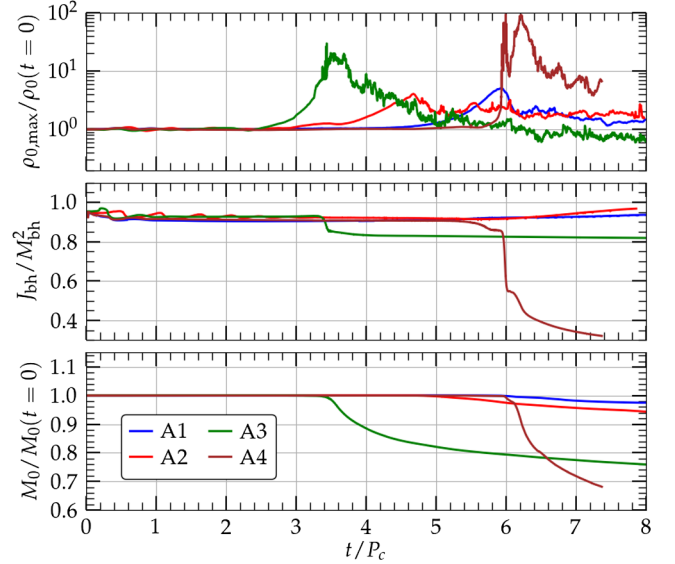

FIG. 10. Evolution of the maximum rest-mass density of the disk (top panel), the BH dimensionless spin (middle panel), and the disk rest mass (bottom panel).

the phase angle ϕ_1 in Fig. 7. Similarly for the cases A2, A3, and A4 the peak times are $\sim \{4.5P_c, 3.5P_c, 6P_c\}$. Depending on the characteristics of the system the maximum density relaxes to values higher or lower than the initial maximum density and leads to persistent emission of gravitational waves. Also, as already discussed, the larger the tilt, the earlier the peak of the maximum density.

In the middle panel of Fig. 10 the dimensionless spin parameter $\chi = J_{\mathrm{bh}}/M_{\mathrm{bh}}^2$ is plotted as a function of time for all our models. We adopt the AHFinderDirect thorn [121] to locate and monitor the apparent horizon, and the isolated horizon formalism [122] to measure the mass of the BH, M_{bh}, and its dimensionless spin parameter χ. For the cases A1 and A4, we also confirm that the Kerr formula for the ratio of the proper polar horizon circumference L_p, to the equatorial one L_e, $L_p/L_e = 4\sqrt{r_+^2 + a^2}E(\frac{a^2}{r_+^2 + a^2})$ [here $E(x)$ is the complete elliptic integral of the second kind, r_+ is the event horizon in Boyer-Lindquist coordinates, and $a = J_{\mathrm{bh}}/M_{\mathrm{bh}}$ is the Kerr spin parameter], and its approximation $L_p/L_e \approx (\sqrt{1 - (a/M_{\mathrm{bh}})^2} + 1.55)/2.55$ [123], yield almost identical results for the evolution of χ. For the tilted case A2 we observe that the BH is spun up and approaches maximum spin, which prevents us from continuing the simulation beyond $\sim$ eight rotation periods. For the 90° tilted case A3 we observe that when the maximum density peaks at $\sim 3.5P_c$ significant accretion onto the BH is initiated, which results in a reduction of the rest mass of the disk (bottom panel in Fig. 10). At the same time the mass of the BH increases (in an analogous way as the decrease of the disk rest mass), which leads to an abrupt decrease of its dimensionless spin to $\chi \sim 0.85$. By the end of our simulation at $\sim 8P_c$ the disk has 75% of its initial
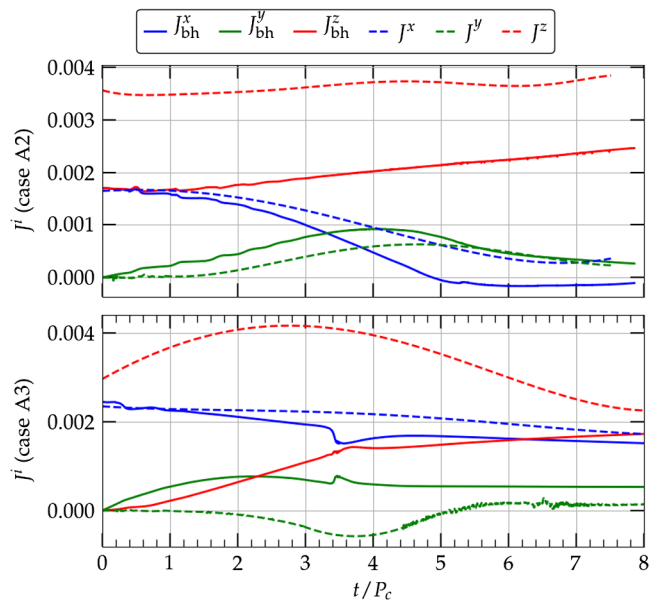
FIG. 11.   Evolution of the BH (solid lines) and ADM (dashed lines) angular momentum components for the tilted cases A2 (45°) and A3 (90°).
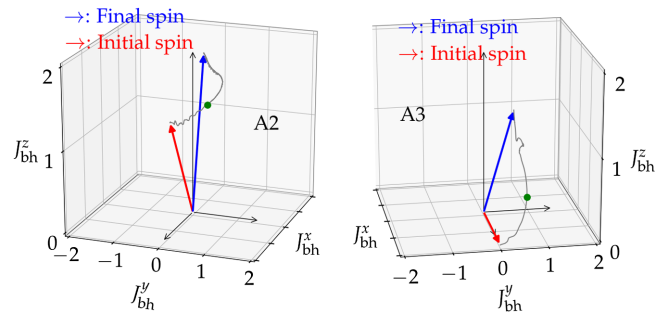

FIG. 12.   BH spin precession for the two tilted cases A2 and A3. The magnitude of the spin vector is not to scale. The gray curve shows the evolution of the spin from its initial value (red arrow) to its final value (blue arrow). Green dots denote times $t = 3P_c$ for model A2, and $t = 2P_c$ for model A3.

mass and the spin of the BH asymptotes to $\chi \sim 0.82$. The most unstable case in our simulations is the antialigned case A4. At six rotation periods the maximum rest-mass density increases by 2 orders of magnitude and shortly afterwards massive accretion is initiated. That increases the BH mass significantly and its spin drops to ~ 0.5. Interestingly, the x and y spin components do not show any appreciable change (i.e. they remain zero); only the z component decreases in magnitude. We did not observe such instability in Ref. [79] where a model with a much smaller spin $\chi = -0.7$ was employed. We plan to investigate this issue in the future. The evolution of the three components of the BH spin as well as the three components of the ADM angular momentum for the two tilted cases A2 and A3 are plotted in Fig. 11. In Fig. 12 we plot the BH spin for the tilted models A2 and A3 as it evolves from its initial value (red arrow) to its final one (blue arrow). The gray curve shows the path of the BH spin vector throughout our simulations. In order to verify that precession is observed and measured well before significant accretion arises, and to accurately measure the GM-induced precession we show a green bullet that corresponds to $t = 3P_c$ for model A2 and $t = 2P_c$ for model A3. Although at those times the PPI is growing (see Figs. 6 and 7) the rest masses of the disks are essentially the same as their initial values. The precession of the BH spin from its initial value (red arrows) to the green bullets is thus mainly due to the GM effect. Projecting the gray path onto the x-y plane and computing its radius of curvature we find that the angle between the projections of the initial spin vector and the spin vector corresponding to the green bullet is $\approx 18°$ or $P_{\mathrm{GM}}/20$, which yields $P_{\mathrm{GM}} \approx 60P_c$. This value exactly matches the

estimate from the analysis of Sec. II A reported in Table I. A similar calculation for model A3 yields an angle between the projections of the initial spin vector and the spin vector corresponding to the green bullet of $\approx 19°$ or $P_{\mathrm{GM}}/19$. Hence $P_{\mathrm{GM}} \approx 38P_c$ which is in excellent agreement with the estimate reported in Table I. Therefore our simulations are in agreement with the estimates from the PN analysis in Sec. II A.

D. Multimessenger astronomy

BHDs are prominent sources of electromagnetic radiation due to accretion. In our case because of the self-gravity of the disk such systems also produce significant amounts of gravitational radiation, which makes them excellent sources for multimessenger astronomy. For the extraction of gravitational waves we measure the outgoing component of the complex Weyl scalar Ψ_4 expanded in terms of the spin-weighted spherical harmonics with spin weight -2 at various finite radii. The axis of the spherical harmonics is taken to be the z axis which is the initial direction of the disk angular momentum. The strain h is then computed with a double integration in time as described in Ref. [124].

In previous studies [76,77,79,80], where nonspinning or aligned BHD systems were analyzed, it was found that the development and saturation of the PPI leads to an initial wave burst, and then a relaxation to a persistent quasimonochromatic signal of lower amplitude. The peak amplitude of the strain depends on the disk-to-BH mass ratio as well as the disk characteristics. Disks of constant specific angular momentum profiles develop a more pronounced $m = 1$ instability, and thus the amplitude of the gravitational wave is larger. As explained in Refs. [79,125] $rh \sim O((r_c \Omega_c)^2)$ and therefore the amplitude of the strain is directly related to the angular velocity and radius of the maximum density point.

When the orbital angular momentum and the BH spin are misaligned this will cause the precession of the orbit and a modulation of the gravitational waves. As we have seen in
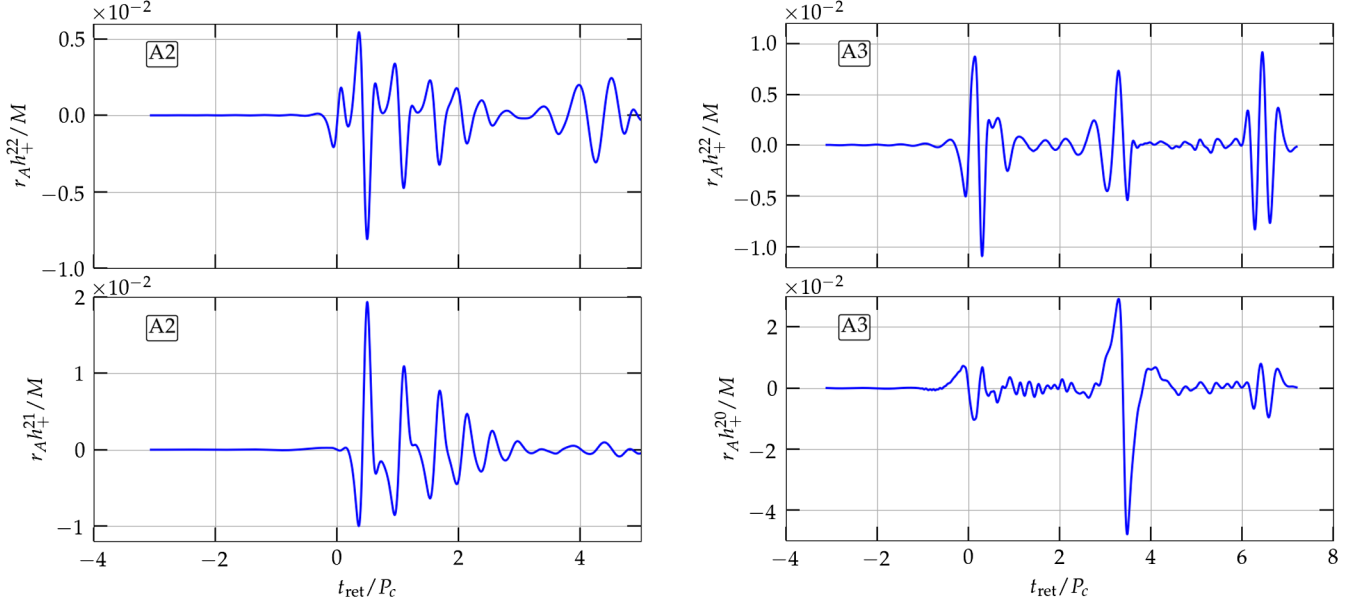
FIG. 13.   Strain amplitude (h_+) for various gravitational-wave modes for the two tilted models A2 and A3. Here r_A is the areal extraction radius and $t_{\rm ret}$ is retarded time.

Sec. II A, the angular velocity of the orbital precession is much smaller than the orbital angular velocity, which implies that we will need many rotation periods to observe the imprint of precession on the gravitational waves. In the left column of Fig. 13 we plot the (2,2) mode (top panel) and (2,1) mode (bottom panel) of h_+ for the tilted case A2 (r_A is the areal extraction radius). As we discussed above we cannot evolve this model beyond eight rotation periods due to the almost extremal spin the BH acquires from accretion. Despite that we observe that the initial amplitude of the strain is much larger than in the aligned cases (see for example Ref. [79]). In this particular model the (2,1) mode has a larger initial amplitude than the (2,2) mode. The reason for this large initial amplitude is not due to the $r_c\Omega_c$ value mentioned above but from the large nonaxisymmetry of the system at $t = 0$. Indeed, the aligned model A1 has the same $r_c\Omega_c$ value as model A2 but it has a much smaller peak strain even though the rest mass of the disk is larger.

Similar large amplitudes are found in the right panels of Fig. 13 where the h_+ strain of the modes (2,2) and (2,0) are plotted for the tilted case A3. The large peak of the (2,0) mode is also present in the (2,1) mode, characteristic of mode mixing. Contrary to the A2 case where the $\ell = 3$ modes are negligible, case A3 has significant amplitude $\ell = 3$ modes. In Ref. [78] where spins up to $\chi \sim 0.5$ and tilt angles up to $\sim 30°$ were employed it was found that the gravitational-wave signal has a weak dependence on the initial tilt angle, especially for disks with nonconstant specific angular momentum profiles. The authors observed the smallest peak amplitudes for the most tilted BH spacetime. By contrast, in our simulations we see that the gravitational-wave signal can be greatly influenced by the tilt angle as discussed above for the cases A2 and A3.

Also, for case A3, which has the largest tilt we observe the largest peak amplitude.

We compute the Fourier power spectrum of the gravitational waves for the (2,2) mode by calculating

$$\tilde{h}(f) = \sqrt{\frac{|\tilde{h}_+^{22}(f)|^2 + |\tilde{h}_\times^{22}(f)|^2}{2}}. \qquad (13)$$

Here $\tilde{h}_+^{22}(f)$ and $\tilde{h}_\times^{22}(f)$ are the Fourier transforms of the two independent polarizations $+$ and $\times$. In left panel of Fig. 14 we plot the dimensionless characteristic strain $h_c(f) = 2f\tilde{h}(f)$ for the four models A1–A4. Cases A1 and A3 have peaks at twice the orbital frequency f_c while case A2 has a peak at approximately $3f_c$ and a secondary one at $2f_c$. The short evolution of the latter, due to reaching maximal spin, reflects mainly the initial spectral content for that model, i.e. for $t_{\rm ret} \lesssim 2P_c$ in the left panels of Fig. 13, where a modulation of the gravitational wave is present. For $t_{\rm ret} \gtrsim 2P_c$ this modulation is smoothed out. We expect that this effect is due to the specific structure of the BHD. As explained in detail in Ref. [79] the gravitational waves depend on the mass of the system from which they originate and will be excellent sources for the future gravitational-wave observatories. In addition, for tilted BHDs the gravitational-wave strain of modes beyond the (2,2) mode is as strong as the (2,2) one (see the bottom row of Fig. 13), and thus the magnitude of their characteristic strain will be comparable to that of Fig. 14 (left panel) and therefore detectable by future gravitational-wave observatories.

In the presence of magnetic fields simulations of compact objects that lead to the formation of BHDs have
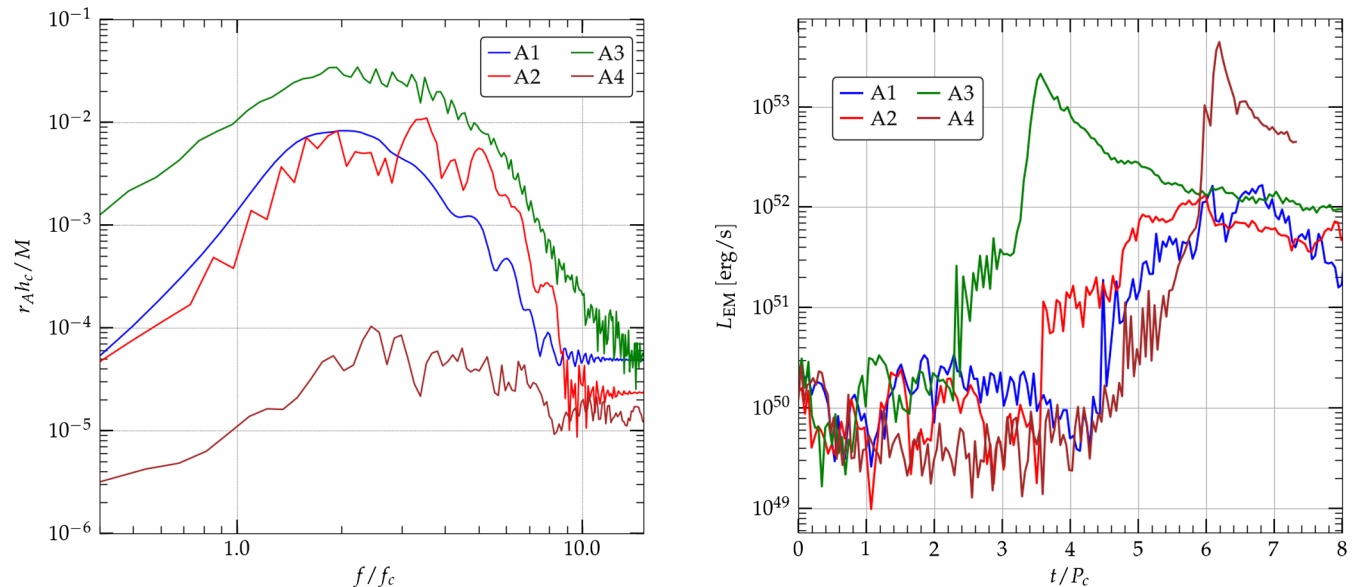
FIG. 14. Left panel: gravitational-wave spectrum of the (2,2) mode. Right panel: estimated bolometric luminosities.

shown that they can power relativistic jets [46–48,126–129] with an outgoing electromagnetic Poynting luminosity of $L_{EM} \sim 10^{52\pm1}$ erg/s. These relativistic jets are consistent with the Blandford-Znajek mechanism for launching jets and their associated Poynting luminosities [130]. Although our simulations lack magnetic fields we can still estimate the Poynting electromagnetic luminosity, since the power available for electromagnetic jet emission is usually proportional to the accretion power [131], i.e.

$$L_{EM} = \epsilon \dot{M}_0 c^2, \tag{14}$$

where $\dot{M}_0$ is the rest-mass accretion rate and ϵ is an efficiency factor of $O(10^{-3})$–$O(10^{-2})$. Assuming $\epsilon = 0.003$ as in Ref. [132] we plot in the right panel of Fig. 14 the electromagnetic luminosity for models A1–A4. The tilted cases A2 and A3 exhibit episodes of accretion at earlier times, due to the tilted geometry of the ISCO. The larger the tilt, the earlier these episodes appear ($2.5P_c$ for A3 and $3.5P_c$ for A2). Following these periods, accretion continues to grow exponentially until approximately the saturation of the PPI, at which point it drops. The tilt seems to affect the asymptotic value of the accretion rate. Although longer simulations are needed for more conclusive results, with radiative transport and magnetic fields incorporated, our simulations show that case A3 asymptotes to a larger value than case A2, which in turn asymptotes to a larger value than case A1, with the differences being less than an order of magnitude. From Fig. 14 we compute the accretion time scale of our models to be $t_{accr} \approx 2 \times 10^4$–$10^5 M_{bh}$ consistent with Refs. [76,79]. Analogous to the accretion rate, the accretion time scales follow $t_{accr}(A1) > t_{accr}(A2) > t_{accr}(A3)$.

On the other hand, the inclusion of magnetic fields will lead to the development of the magnetorotational instability [133] as well as turbulence [134]. The increase of turbulent viscosity will redistribute the angular momentum in the disk with the possibility of suppressing the PPI. Despite this, if the turbulent viscous time scale is much longer than the time scale for the growth and saturation of the PPI there may be sufficient time for a multimessenger event. We estimate the viscous time scale as

$$\frac{\tau_{vis}}{P_c} = \frac{R^2}{P_c \nu} \approx \frac{1}{2\pi\alpha} \frac{\Omega_c R^2}{c_s H} \tag{15}$$

where $\nu = \alpha H c_s$ is the shear viscosity, (H, R) are the (height, width) of the disk, c_s is the sound speed, and α is the Shakura-Sunyaev viscosity parameter [4]. In our case $c_s^2 = \Gamma(\Gamma - 1)P/((\Gamma - 1)\rho + \Gamma P)$. For $\alpha = 0.01$ it turns out that our models have $\tau_{vis}/P_c \sim \{198, 198, 201, 176\}$. Even if α_{SS} is 5 times larger, the viscous time scale will be $\sim 40 P_c$ i.e. much larger than the time for PPI development and saturation. This is especially true for the tilted BHDs, in which case the PPI grows much earlier than in the aligned/antialigned ones. Therefore our preliminary conclusion is that the one-arm instability in BHD systems can still be a source for multimessenger astronomy. Full general-relativistic magnetohydrodynamic simulations with radiative transport will be needed to reliably assess the outcome of such systems.

IV. DISCUSSION

In this work we initiated a study of tilted, self-gravitating disks around spinning black holes. Our general-relativistic, hydrodynamics simulations are the first that start from

self-consistent initial values and include highly spinning black holes. In these preliminary simulations we focused on BHDs that have a constant specific angular momentum profile and for which the disk-to-BH mass ratio is 16–28%. We investigated aligned (0°), antialigned (180°), and highly tilted systems (45° and 90°), all of them having dimensionless spins of 0.96–0.97. The nonaxisymmetric mode analysis showed that the saturation of the PPI happens earlier than in the aligned/antialigned cases and the $m = 1$ mode growth is smaller. The disks precess and warp around the BHs, which also precess following PN GM precession periods. This causes the BH center to acquire a small kick velocity. We confirmed that after outward angular momentum transport is initiated close to the $m = 1$ corotation radius, the disk's maximum density increases (sometimes by orders of magnitude). Accretion on the BH causes its dimensionless spin either to increase or to decrease, depending on the configuration. In the 90° initial tilt case, we found an alignment of the disk with the BH spin similar to Refs. [7,67,115,116]. This alignment should not be interpreted as a BP effect for multiple reasons. 1) Our disks have $H/R = 0.625 \gg \alpha$ (effective α) in contrast to the condition $H/R \ll \alpha$ that the BP effect is known to operate. Here we have no explicit viscosity. 2) Global alignment arises, and not just alignment near the BH. 3) In addition to 2) the inner parts of the disk that create the plunging streams on the BH are not perpendicular to the BH spin, typical of the BP picture. 4) The alignment happens on a time scale much shorter than the effective viscous time scale estimated in Sec. III D. Tilted systems exhibit earlier accretion episodes than the aligned/antialigned ones. We also observed a weak dependence on the BH tilt, with larger tilts leading to higher accretion rates, although longer simulations are needed. Gravitational waves from tilted BHDs typically have larger strains than the ones coming from aligned/antialigned systems and exhibit a diverse spectrum of modes beyond the (2,2) mode. We expect such self-gravitating disks to be excellent sources for multimessenger astronomy.

[1] S. E. Woosley, Astrophys. J. **405,** 273 (1993).

[2] A. I. MacFadyen and S. E. Woosley, Astrophys. J. **524,** 262 (1999).

[3] D. Lynden-Bell, Nature (London) **223,** 690 (1969).

[4] N. I. Shakura and R. A. Sunyaev, Astron. Astrophys. **24,** 337 (1973).

[5] B. Paczynski, Acta Astron. **28,** 91 (1978).

[6] T. Fragos, M. Tremmel, E. Rantsiou, and K. Belczynski, Astrophys. J. Lett. **719,** L79 (2010).

[7] M. Liska, C. Hesp, A. Tchekhovskoy, A. Ingram, M. van der Klis, and S. Markoff, Mon. Not. R. Astron. Soc. **474,** L81 (2018).

[8] R. D. Blandford and R. L. Znajek, Mon. Not. R. Astron. Soc. **179,** 433 (1977).

[9] R. D. Blandford and D. G. Payne, Mon. Not. R. Astron. Soc. **199,** 883 (1982).

[10] S. Aalto, F. Costagliola, S. Muller, K. Sakamoto, J. S. Gallagher, K. Dasyra, K. Wada, F. Combes, S. García-Burillo, L. E. Kristensen, S. Martín, P. van der Werf, A. S. Evans, and J. Kotilainen, Astron. Astrophys. **590,** A73 (2016).

[11] Z. Abraham, Nat. Astron. **2,** 443 (2018).

[12] P. C. Fragile, G. J. Mathews, and J. R. Wilson, Astrophys. J. **553,** 955 (2001).

[13] R. M. Hjellming and M. P. Rupen, Nature (London) **375,** 464 (1995).

[14] J. Greene, C. D. Bailyn, and J. A. Orosz, Astrophys. J. **554,** 1290 (2001).

[15] T. J. Maccarone, Mon. Not. R. Astron. Soc. **336,** 1371 (2002).

[16] A. Caproni, M. Livio, Z. Abraham, and H. J. M. Cuesta, Astrophys. J. **653,** 112 (2006).

[17] T. D. Russell et al., Astrophys. J. **883,** 198 (2019).

[18] K. Akiyama et al. (Event Horizon Telescope Collaboration), Astrophys. J. Lett. **875,** L1 (2019).

[19] K. Chatterjee, Z. Younsi, M. Liska, A. Tchekhovskoy, S. B. Markoff, D. Yoon, D. van Eijnatten, C. Hesp, A.

Ingram, and M. van der Klis, Mon. Not. R. Astron. Soc. **499,** 362 (2020).

[20] J. Park, K. Hada, M. Kino, M. Nakamura, H. Ro, and S. Trippe, Astrophys. J. **871,** 257 (2019).

[21] F. Foucart, M. D. Duez, L. E. Kidder, and S. A. Teukolsky, Phys. Rev. D **83,** 024005 (2011).

[22] F. Foucart, M. Deaton, M. D. Duez, L. E. Kidder, I. MacDonald, C. D. Ott, H. P. Pfeiffer, M. A. Scheel, B. Szilagyi, and S. A. Teukolsky, Phys. Rev. D **87,** 084006 (2013).

[23] K. Kawaguchi, K. Kyutoku, H. Nakano, H. Okawa, M. Shibata, and K. Taniguchi, Phys. Rev. D **92,** 024014 (2015).

[24] T. Dietrich, S. Bernuzzi, B. Brügmann, M. Ujevic, and W. Tichy, Phys. Rev. D **97,** 064002 (2018).

[25] S. V. Chaurasia, T. Dietrich, M. Ujevic, K. Hendriks, R. Dudi, F. M. Fabbri, W. Tichy, and B. Brügmann, Phys. Rev. D **102,** 024087 (2020).

[26] K. Belczynski, R. E. Taam, E. Rantsiou, and M. van der Sluys, Astrophys. J. **682,** 474 (2008).

[27] J. Lense and H. Thirring, Phys. Z. **19,** 156 (1918).

[28] J. M. Bardeen and J. A. Petterson, Astrophys. J. **195,** L65 (1975).

[29] J. C. B. Papaloizou and J. E. Pringle, Mon. Not. R. Astron. Soc. **202,** 1181 (1983).

[30] S. H. Lubow, G. I. Ogilvie, and J. E. Pringle, Mon. Not. R. Astron. Soc. **337,** 706 (2002).

[31] N. Stone and A. Loeb, Phys. Rev. Lett. **108,** 061302 (2012).

[32] M. van der Klis, Astron. Nachr. **326,** 798 (2005).

[33] L. Stella and M. Vietri, Astrophys. J. Lett. **492,** L59 (1998).

[34] D. Marković and F. K. Lamb, Astrophys. J. **507,** 316 (1998).

[35] A. Ingram, C. Done, and P. C. Fragile, Mon. Not. R. Astron. Soc. **397,** L101 (2009).

[36] A. Ingram and S. Motta, New Astron. Rev. **85,** 101524 (2019).

[37] G. Musoke, M. Liska, O. Porth, M. van der Klis, and A. Ingram, arXiv:2201.03085.

[38] R. Y. Talbot, M. A. Bourne, and D. Sijacki, Mon. Not. R. Astron. Soc. **504,** 3619 (2021).

[39] M. A. Abramowicz, M. Calvani, and L. Nobili, Nature (London) **302,** 597 (1983).

[40] J. A. Font and F. Daigne, Mon. Not. R. Astron. Soc. **334,** 383 (2002).

[41] F. Daigne and J. A. Font, Mon. Not. R. Astron. Soc. **349,** 841 (2004).

[42] O. Korobkin, E. Abdikamalov, N. Stergioulas, E. Schnetter, B. Zink, S. Rosswog, and C. D. Ott, Mon. Not. R. Astron. Soc. **431,** 349 (2013).

[43] L. Rezzolla, L. Baiotti, B. Giacomazzo, D. Link, and J. A. Font, Classical Quantum Gravity **27,** 114105 (2010).

[44] K. Hotokezaka, K. Kiuchi, K. Kyutoku, H. Okawa, Y.-i. Sekiguchi, M. Shibata, and K. Taniguchi, Phys. Rev. D **87,** 024001 (2013).

[45] V. Paschalidis, M. Ruiz, and S. L. Shapiro, Astrophys. J. **806,** L14 (2015).

[46] M. Ruiz, R. N. Lang, V. Paschalidis, and S. L. Shapiro, Astrophys. J. **824,** L6 (2016).

[47] M. Ruiz, S. L. Shapiro, and A. Tsokaros, Phys. Rev. D **98,** 123017 (2018).

[48] M. Ruiz, A. Tsokaros, and S. L. Shapiro, Phys. Rev. D **104,** 124049 (2021).

[49] J. C. B. Papaloizou and J. E. Pringle, Mon. Not. R. Astron. Soc. **208,** 721 (1984).

[50] O. M. Blaes and W. Glatzel, Mon. Not. R. Astron. Soc. **220,** 253 (1986).

[51] S. A. Balbus, Annu. Rev. Astron. Astrophys. **41,** 555 (2003).

[52] J. C. B. Papaloizou and J. E. Pringle, Mon. Not. R. Astron. Soc. **213,** 799 (1985).

[53] W. H. Zurek and W. Benz, Astrophys. J. **308,** 123 (1986).

[54] P. Goldreich, J. Goodman, and R. Narayan, Mon. Not. R. Astron. Soc. **221,** 339 (1986).

[55] O. M. Blaes, Mon. Not. R. Astron. Soc. **227,** 975 (1987).

[56] J. F. Hawley, Mon. Not. R. Astron. Soc. **225,** 677 (1987).

[57] J. Goodman, R. Narayan, and P. Goldreich, Mon. Not. R. Astron. Soc. **225,** 695 (1987).

[58] J. F. Hawley, Astrophys. J. **381,** 496 (1991).

[59] J. C. B. Papaloizou and D. N. C. Lin, Annu. Rev. Astron. Astrophys. **33,** 505 (1995).

[60] J. Goodman and R. R. Rafikov, Astrophys. J. **552,** 793 (2001).

[61] T. Heinemann and J. C. B. Papaloizou, Mon. Not. R. Astron. Soc. **419,** 1085 (2012).

[62] S. Chandrasekhar, Astrophys. J. **161,** 561 (1970).

[63] J. L. Friedman and B. F. Schutz, Astrophys. J. **221,** 937 (1978).

[64] J. L. Friedman, Commun. Math. Phys. **62,** 247 (1978).

[65] J.-P. De Villiers and J. F. Hawley, Astrophys. J. **577,** 866 (2002).

[66] O. M. Blaes and J. F. Hawley, Astrophys. J. **326,** 277 (1988).

[67] P. C. Fragile and P. Anninos, Astrophys. J. **623,** 347 (2005).

[68] R. P. Nelson and J. C. B. Papaloizou, Mon. Not. R. Astron. Soc. **315,** 570 (2000).

[69] R. Nealon, D. J. Price, and C. J. Nixon, Mon. Not. R. Astron. Soc. **448,** 1526 (2015).

[70] P. B. Ivanov and A. F. Illarionov, Mon. Not. R. Astron. Soc. **285,** 394 (1997).

[71] M. Demianski and P. B. Ivanov, Astron. Astrophys. **324,** 829 (1997).

[72] G. I. Ogilvie, Mon. Not. R. Astron. Soc. **304,** 557 (1999).

[73] F. Foucart, Phys. Rev. D **86,** 124007 (2012).

[74] G. Lovelace, M. D. Duez, F. Foucart, L. E. Kidder, H. P. Pfeiffer *et al.*, Classical Quantum Gravity **30,** 135004 (2013).

[75] P. J. Montero, J. A. Font, and M. Shibata, Phys. Rev. Lett. **104,** 191101 (2010).

[76] K. Kiuchi, M. Shibata, P. J. Montero, and J. A. Font, Phys. Rev. Lett. **106,** 251102 (2011).

[77] V. Mewes, J. A. Font, F. Galeazzi, P. J. Montero, and N. Stergioulas, Phys. Rev. D **93,** 064055 (2016).

[78] V. Mewes, F. Galeazzi, J. A. Font, P. J. Montero, and N. Stergioulas, Mon. Not. R. Astron. Soc. **461,** 2480 (2016).

[79] E. Wessel, V. Paschalidis, A. Tsokaros, M. Ruiz, and S. L. Shapiro, Phys. Rev. D **103,** 043013 (2021).

[80] M. Shibata, K. Kiuchi, S. Fujibayashi, and Y. Sekiguchi, Phys. Rev. D **103**, 063037 (2021).

[81] R. D. Ekers, R. Fanti, C. Lari, and P. Parma, Nature (London) **276**, 588 (1978).

[82] C. C. Cheung, Astron. J. **133**, 2097 (2007).

[83] S. Bera, S. Pal, T. K. Sasmal, and S. Mondal, Astrophys. J. Suppl. Ser. **251**, 9 (2020).

[84] O. Korobkin, E. B. Abdikamalov, E. Schnetter, N. Stergioulas, and B. Zink, Phys. Rev. D **83**, 043007 (2011).

[85] M. Shibata, K. Kiuchi, S. Fujibayashi, and Y. Sekiguchi, Phys. Rev. D **103**, 063037 (2021).

[86] J. Goodman and R. Narayan, Mon. Not. R. Astron. Soc. **231**, 97 (1988).

[87] J. C. B. Papaloizou and D. N. C. Lin, Astrophys. J. **344**, 645 (1989).

[88] J. E. Tohline and I. Hachisu, Astrophys. J. **361**, 394 (1990).

[89] D. M. Christodoulou and R. Narayan, Astrophys. J. **388**, 451 (1992).

[90] D. M. Christodoulou, Astrophys. J. **412**, 696 (1993).

[91] N. Stergioulas, Int. J. Mod. Phys. D **20**, 1251 (2011).

[92] A. Tsokaros, K. Uryu, and S. L. Shapiro, Phys. Rev. D **99**, 041501 (2019).

[93] A. A. Tsokaros and K. Uryū, Phys. Rev. D **75**, 044026 (2007).

[94] S. K. Chakrabarti, Astrophys. J. **288**, 1 (1985).

[95] J.-P. D. Villiers, J. F. Hawley, and J. H. Krolik, Astrophys. J. **599**, 1238 (2003).

[96] A. Ashtekar and B. Krishnan, Living Rev. Relativity **7**, 10 (2004).

[97] O. Dreyer, B. Krishnan, D. Shoemaker, and E. Schnetter, Phys. Rev. D **67**, 024018 (2003).

[98] D. Christodoulou, Phys. Rev. Lett. **25**, 1596 (1970).

[99] K. S. Thorne, R. H. Price, and D. A. Macdonald, *The Membrane Paradigm* (Yale University Press, New Haven, 1986).

[100] H. von Zeipel, Mon. Not. R. Astron. Soc. **84**, 665 (1924).

[101] J.-L. Tassoul, *Theory of Rotating Stars* (Princeton University Press, Princeton, NJ, 1978).

[102] M. A. Abramowicz, Acta Astron. **24**, 45 (1974).

[103] J. Karkowski, W. Kulczycki, P. Mach, E. Malec, A. Odrzywołek, and M. Piróg, Phys. Rev. D **97**, 104017 (2018).

[104] M. Shibata and T. Nakamura, Phys. Rev. D **52**, 5428 (1995).

[105] T. W. Baumgarte and S. L. Shapiro, Phys. Rev. D **59**, 024007 (1998).

[106] Z. B. Etienne, J. A. Faber, Y. T. Liu, S. L. Shapiro, K. Taniguchi, and T. W. Baumgarte, Phys. Rev. D **77**, 084002 (2008).

[107] E. Schnetter, S. H. Hawley, and I. Hawke, Classical Quantum Gravity **21**, 1465 (2004).

[108] Carpet, Carpet Code homepage.

[109] J. G. Baker, J. Centrella, D.-I. Choi, M. Koppitz, and J. van Meter, Phys. Rev. D **73**, 104002 (2006).

[110] M. D. Duez, P. Marronetti, S. L. Shapiro, and T. W. Baumgarte, Phys. Rev. D **67**, 024004 (2003).

[111] C. A. Raithel and V. Paschalidis, Phys. Rev. D **106**, 023015 (2022).

[112] Z. B. Etienne, V. Paschalidis, Y. T. Liu, and S. L. Shapiro, Phys. Rev. D **85**, 024013 (2012).

[113] Z. B. Etienne, Y. T. Liu, and S. L. Shapiro, Phys. Rev. D **82**, 084031 (2010).

[114] M. Liska, A. Tchekhovskoy, A. Ingram, and M. van der Klis, Mon. Not. R. Astron. Soc. **487**, 550 (2019).

[115] P. C. Fragile, O. M. Blaes, P. Anninos, and J. D. Salmonson, Astrophys. J. **668**, 417 (2007).

[116] J. Dexter and P. C. Fragile, Astrophys. J. **730**, 36 (2011).

[117] S. A. Hughes, Phys. Rev. D **64**, 064004 (2001); **88**, 109902(E) (2013).

[118] V. Paschalidis, W. E. East, F. Pretorius, and S. L. Shapiro, Phys. Rev. D **92**, 121502 (2015).

[119] H. A. Williams and J. E. Tohline, Astrophys. J. **315**, 594 (1987).

[120] J. W. Woodward, J. E. Tohline, and I. Hachisu, Astrophys. J. **420**, 247 (1994).

[121] J. Thornburg, Classical Quantum Gravity **21**, 743 (2004).

[122] O. Dreyer, B. Krishnan, D. Shoemaker, and E. Schnetter, Phys. Rev. D **67**, 024018 (2003).

[123] S. R. Brandt and E. Seidel, Phys. Rev. D **52**, 870 (1995).

[124] C. Reisswig and D. Pollney, Classical Quantum Gravity **28**, 195015 (2011).

[125] D. Lai, F. A. Rasio, and S. L. Shapiro, Astrophys. J. **423**, 344 (1994).

[126] V. Paschalidis, M. Ruiz, and S. L. Shapiro, Astrophys. J. Lett. **806**, L14 (2015).

[127] M. Ruiz, S. L. Shapiro, and A. Tsokaros, Phys. Rev. D **97**, 021501 (2018).

[128] M. Ruiz, A. Tsokaros, V. Paschalidis, and S. L. Shapiro, Phys. Rev. D **99**, 084032 (2019).

[129] L. Sun, M. Ruiz, S. L. Shapiro, and A. Tsokaros, Phys. Rev. D **105**, 104028 (2022).

[130] R. D. Blandford and R. L. Znajek, Mon. Not. R. Astron. Soc. **179**, 433 (1977).

[131] S. L. Shapiro and S. A. Teukolsky, *Black Holes, White Dwarfs, and Neutron Stars* (John Wiley & Sons, New York, 1983).

[132] M. Ruiz, A. Tsokaros, and S. L. Shapiro, Phys. Rev. D **101**, 064042 (2020).

[133] S. A. Balbus and J. F. Hawley, Astrophys. J. **376**, 214 (1991).

[134] M. Bugli, J. Guilet, E. Müller, L. Del Zanna, N. Bucciantini, and P. J. Montero, Mon. Not. R. Astron. Soc. **475**, 108 (2018).